ESS Report 03-138-A
August, 2003

Revised ESS Front-End (2.5 - 20 MeV)

Frank Gerigk

Accelerator Theory & Future Projects Group
CCLRC Rutherford Appleton Laboratory, Chilton, Didcot, Oxon, UK

Abstract. This paper reports on changes in the 280 MHz normal-conducting ESS front-end. The first two DTL tanks have been redesigned with a larger bore radius and an FFDD focusing structure, instead of the previously used FD lattice. The benefits of this measure are outlined, together with some minor changes in the chopping line. Realistic particle tracking with the simulated RFQ output beam is then used to study the effect of random RF phase and gradient errors as well as the effect of random quadrupole gradient errors.

INTRODUCTION

One of the main concerns for the operation of the ESS linac is to keep beam loss below the 1 W/m, a limit that, according to experience at LANL, ensures hands-on maintenance for the machine. Losses are often a result of beam halo that builds up from initial mismatch or mismatch at transitions between different focusing structures. Maximum particle radii created by strong initial mismatch can extend beyond 10 times their r.m.s. values ([1], [2]) and thus fall outside the acceptance of most normal-conducting accelerating structures. Statistically distributed errors can yield r.m.s. beam deviations similar to initial mismatch and might also be an additional source of halo particles [3]. It is thus imperative to study the influence of statistical errors on beam loss and to ensure that the losses remain within the acceptable limit.

In Alvarez Drift Tube Linacs (DTL) the maximum aperture radius is dictated by the required magnetic and electric fields. In practice, geometrical constraints limit the magnetic tip field to approximately 0.6 T, a value that changes little with the actual choice for the inner quadrupole radius. The selection of a large bore radius will therefore result in a low magnetic gradient and a corresponding drop in RF efficiency due to a lower concentration of electric fields on the beam axis.

To overcome the limitation imposed by the quadrupole gradient one can use longer focusing periods, for instance FFDD instead of the standard FD focusing. In that case the same quadrupole gradient provides a ≈ 1.4 times higher

TABLE 1. Input beam parameters for long and short pulse operation.

	short pulse	**long pulse**	
ion species	H^-		
input energy	2.497		MeV
peak current	57		mA
mean current during pulse	40	40/57	mA
beam duty cycle	4.8	3.3	%
repetition rate	50	16.66	Hz
RF frequency	280		MHz
r.m.s. normalized transverse emittance*	0.2054 (x) 0.2034 (y)		π mm mrad
r.m.s. longitudinal emittance*	0.4222		π mm mrad
	0.1333		π deg MeV

* at the input of the MEBT

zero current phase advance per meter. Comparing the full current tunes per meter, the gain is even higher, which was the motivation to change the focusing structure of the ESS DTL to FFDD focusing and thus being able to use a larger bore radius.
Apart from the transverse losses, the phase and energy jitter resulting from small variations of the RF power supplies can severely limit the ultimate machine performance. These errors are of little concern for long pulse operation where the linac beam is directly dumped onto a target. Here, the only critical area is the frequency transition at the beam funnel which is sensitive to variations in phase and energy. For short pulse operation, with the linac beam being injected into subsequent ring systems, a tight control of phase and energy jitter is essential to avoid large injection losses.

MEDIUM ENERGY BEAM TRANSPORT (MEBT)

The proposed MEBT structure is based on the previously reported ESS design [4], but uses four chopper plates instead of two, as depicted in Fig. 1. Minor modifications were applied to the cavity voltages and the settings of the quadrupoles at the input and output of the MEBT in order to match the beam from the RFQ into the MEBT and then into the subsequent DTL. The parameters for the 13 quadrupoles and 6 RF gaps are listed in Table 2 in the Appendix.

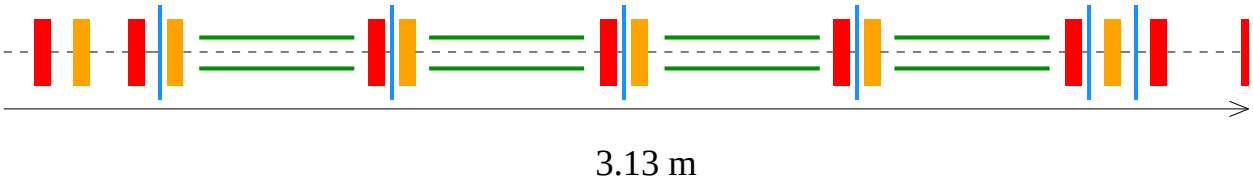

FIGURE 1. Layout of MEBT

Using the simulated RFQ output distribution, the beam loss on the chopper plates amounts to ≈ 1.6% for a chopper plate distance of 14 mm and to ≈ 0.4% for a distance of 16 mm. Apertures above 17 mm reduce the beam loss to almost zero (see Fig. 12). For the simulations in this report an aperture of 16 mm was chosen, meaning that due to the increased voltage requirement the plates will probably have to be lengthened by ≈ 5-10% for a future revision of the MEBT.

DTL DESIGN

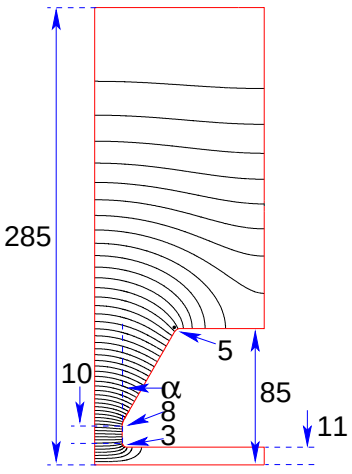

FIGURE 2. DTL half cell.

Due to its compact design, combining quadrupoles and RF gaps in one structure, a DTL is still considered to be the most suitable normal-conducting device to accelerate the beam after the MEBT. An RFQ would use the RF power less efficiently and a coupled cavity drift tube linac (CCDTL) would not be practical since one needs a distance of either $\frac{3}{2}$ or $\frac{5}{2}$ $\beta\lambda$ between neighboring gaps of neighboring tanks (compare [5]). The $\frac{3}{2}$ $\beta\lambda$ option does not provide enough space for a quadrupole between the tanks and the $\frac{5}{2}$ $\beta\lambda$ option would reduce the acceleration efficiency per meter to an unacceptably low level. Furthermore the number of gaps per tank is severely limited by the longitudinal phase advance per period. Other structures, like uncoupled multi-gap tanks with quadrupoles in between (e.g. SDTL), require a large number of RF systems or, a complicated RF distribution network, both of which would raise the cost and the probability of hardware failure.
The RF properties of the ESS-DTL tanks were optimized using the SUPERFISH [6] wrapper DTL_GEN [7]. All quoted shunt impedances are reduced by 20% with respect to the calculated values to account for imperfections (the previous design quoted shunt impedances, reduced by 10%).
The two Alvarez DTL tanks raise the energy from 2.497 to 20.347 MeV and share a common vacuum vessel to avoid a “missing gap” in longitudinal focusing at the transition of the two tanks. All 77 drift tube shapes are based on the same dimensions for inner and outer diameter, corner radii, stem diameter, and flat

length as shown in Fig. 2. The flat surface facing neighboring drift tubes was introduced to ease the machining and alignment of the tubes. The frequency in each cell is adjusted using the drift tube face angle α and the gap length, which vary from 13° to 30° and from 8 to 35 mm, respectively (see Fig. 17 in the Appendix). The peak electric field densities occur on the inner nose tips and are adjusted to a level of 1.3 Kilpatrick throughout the two tanks. Although the shunt impedance of the new structure is much lower than for the previous design [4], the power consumption is still at almost the same level. This is achieved by reducing the electric field strength in the tanks, now starting at 1.8 MeV/m and then being linearly increased to a maximum level of 2.5 MeV/m at the end of tank 2. A linear ramp is also applied to the synchronous phase which is raised from -42° to -30°. Post couplers will be used for field stabilization in the tanks. Two 1.3 MW klystrons deliver a total power of 1.1 MW to each of the two DTL tanks, providing a margin of $\approx$ 20% control power to stabilize the electric field levels during operation. Dividing the beam power by the total power yields an RF efficiency of $\approx$ 0.33 for both tanks.
Figure 3 shows the evolution of the effective shunt impedance[1] and the transit time factor. Table 3 in the Appendix summarizes the DTL parameters.

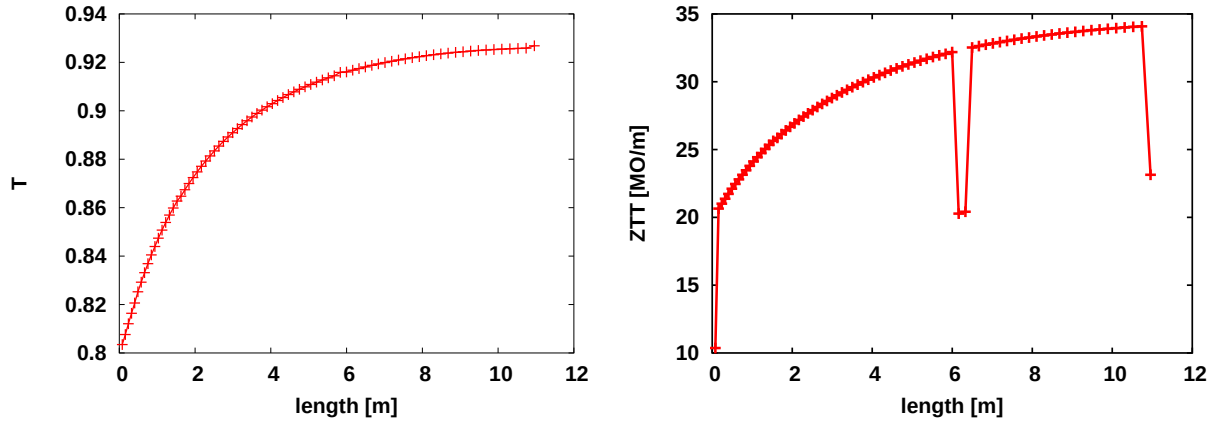

FIGURE 3. Left: transit time factor; **right:** effective shunt impedance

The lower shunt impedance values at the first and last cells of each tank are caused by the losses on the end-walls. Compared to the previous design the new structure is $\approx$ 1.5 m longer, has a bore radius of 11 mm instead of 6.5 mm, and needs 1.1 MW per tank instead of 1 MW. The advantages of the larger bore radius are detailed in the following.

BEAM DYNAMICS WITHOUT ERRORS

The transverse quadrupole settings are determined by two critera: keeping the zero current phase advance per period in each plane below 90° and avoiding unstable regions in Hofmann's stability chart [8] in order to avoid emittance exchange between the longitudinal and the transverse plane. For the ESS DTL coupling can be avoided or, at least minimised, by keeping the full current tune ratio below $\approx$ 0.8 as shown in the chart in Fig. 4.
Figure 5 shows the resulting full current phase advance per meter and the r.m.s. emittance evolution along the MEBT and DTL, both calculated with IMPACT [9].
Clearly, the MEBT introduces an abrupt distortion of the otherwise relatively smooth focusing forces, thus giving rise to a slight emittance growth. One can also observe the onset of emittance exchange, starting in the MEBT and ending in the first DTL tank. An optimisation of the quadrupole settings in the MEBT and a slight decrease of longitudinal focusing in the first periods of the DTL should improve the situation.
Eventually, Fig. 6 depicts the r.m.s. beam sizes in all three planes for a matched beam without lattice errors, and Fig. 7 shows the corresponding output phase space. In both DTL tanks the ratio between the transverse r.m.s. beam radius and the aperture radius of the drift tubes (11 mm) now amounts to $\approx$ 6.5 instead of 4.6 as for the old FD structure proposed in [4]. Moreover the quadrupole tip field is now reduced from 0.65 T to 0.55 T. Using the more ambitious tip field estimate of 0.65 T one could increase the aperture radius of the drift tubes even more (13 mm),

[1] linac definition: $ZT^2 = (E_0 T)^2/(P/l_c)$

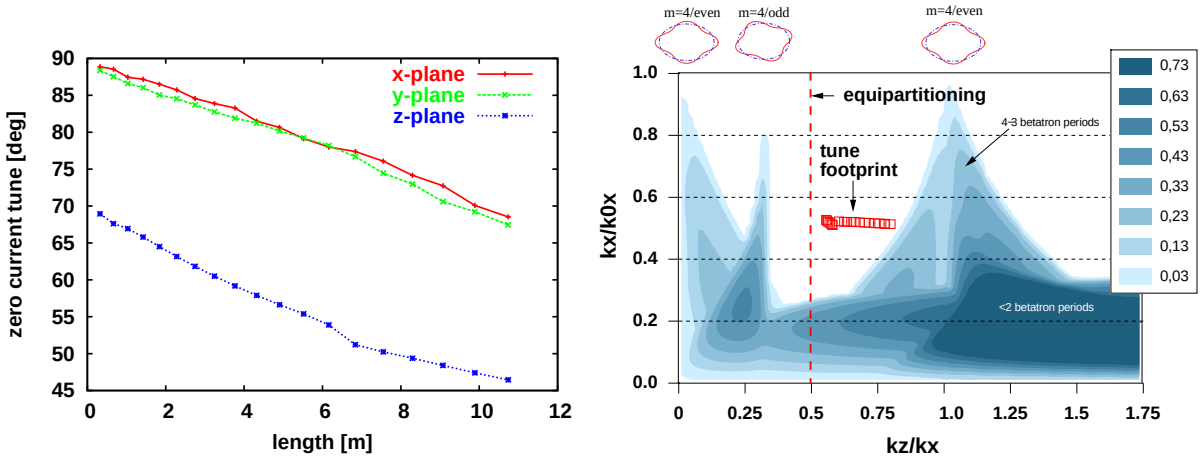

FIGURE 4. **Left:** matched zero current phase advance per period (from envelope code); **right:** instability chart for an emittance ratio of $\varepsilon_l/\varepsilon_t = 2$ with the tune footprint of the ESS DTL.

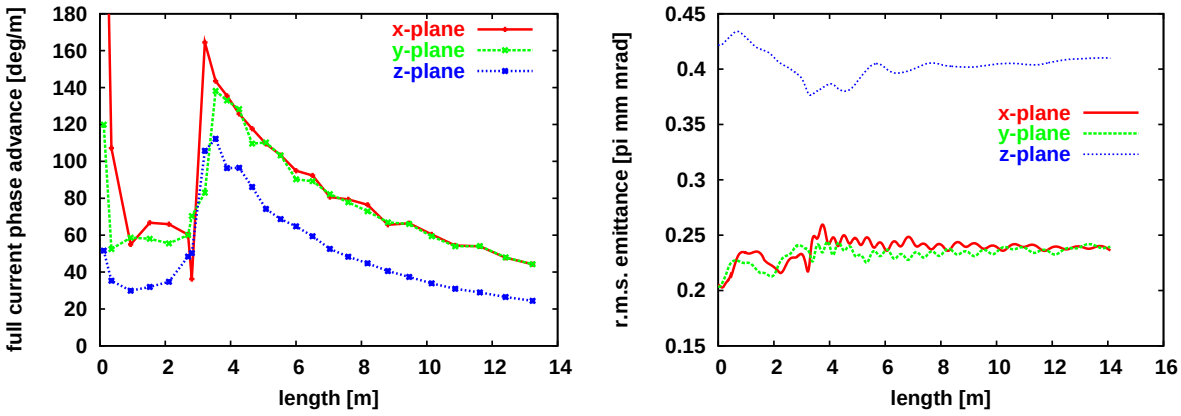

FIGURE 5. **Left:** full current phase advance per meter along MEBT and DTL (from tracking); **right:** r.m.s. emittance evolution along MEBT and DTL. IMPACT simulation using the simulated RFQ output distribution.

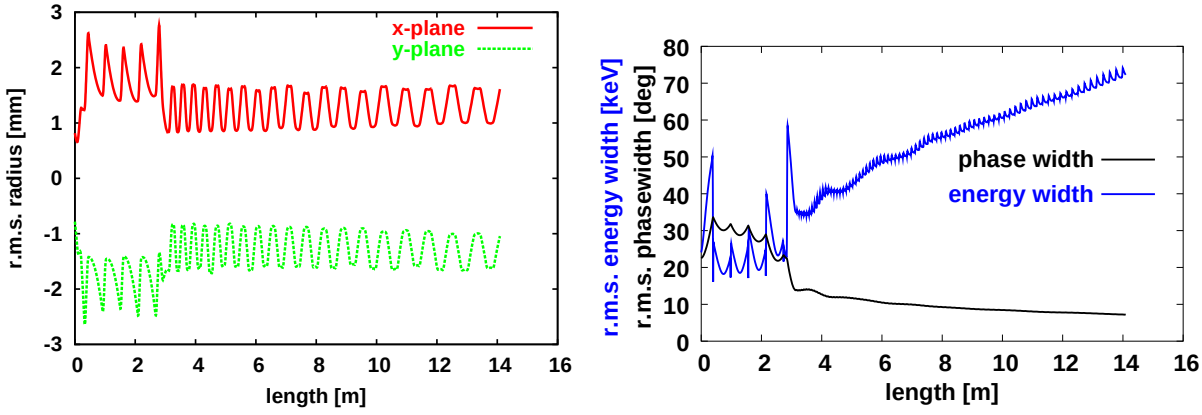

FIGURE 6. **Left:** r.m.s. beam sizes along MEBT and DTL (from tracking); **right:** total r.m.s. phase and energy width along MEBT and DTL. IMPACT simulation using the simulated RFQ output distribution.

offering an increased safety ratio of 7.5. As a guideline one can compare these values with those chosen for the SNS DTL. The FFODDO focusing lattice which provides empty drift tubes for steering and diagnostics has a safety ratio of 6 between r.m.s. beam radius and the beam pipe. However, one should keep in mind that the SNS operates with half the beam current, and transports five times lower beam power in the first DTL sections. Considering that theory predicts halo radii of up to 8-12 times the r.m.s. radii we deem it necessary to provide at least a ratio of 6.5 to ensure hands-on-maintenance for the linac.
Comparisons of simulations with FD and FFDD focusing lattices for the ESS DTL resulted in approximately equal emittance growth values and are not reported in further detail.

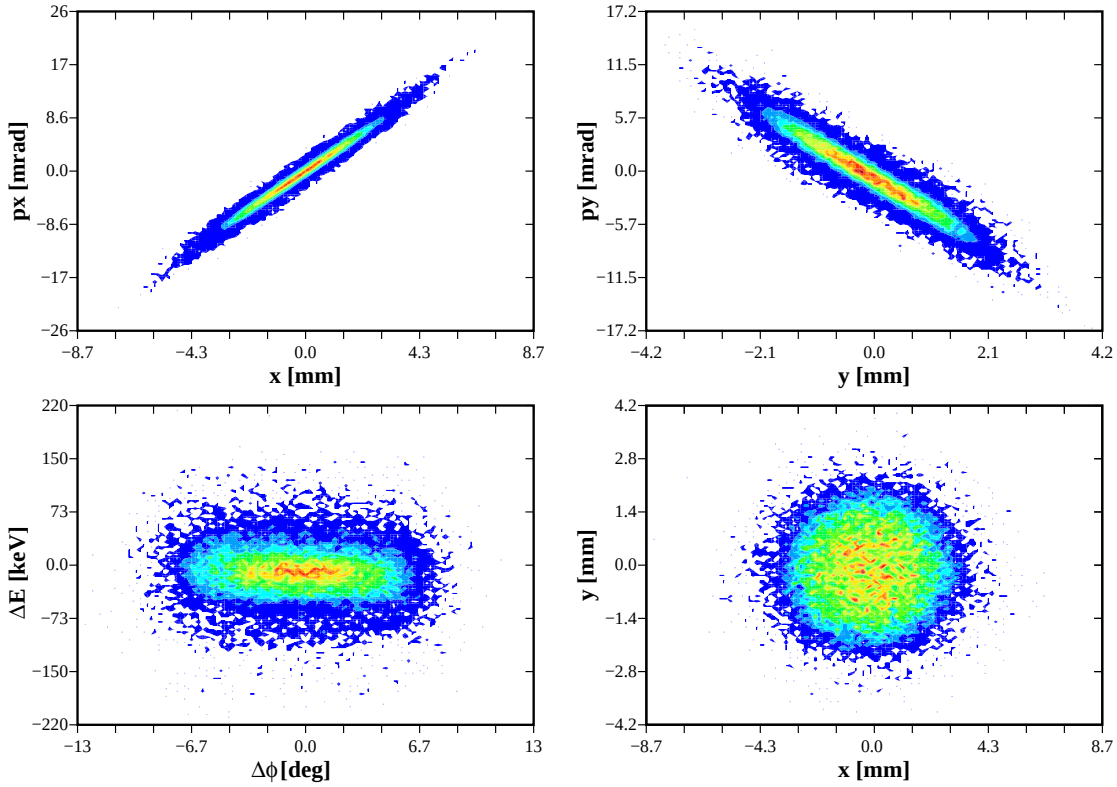

FIGURE 7. Phase space at the output of the DTL (tracking from RFQ input).

BEAM DYNAMICS WITH STATISTICAL ERRORS

This section contains excerpts of the recently published paper [3], which covers statistical errors in the ESS front-end as well as in the Linac4 front-end [5]. In the following we use the classic distinction between 'dynamic' errors that change from pulse to pulse or within single RF pulses, and 'static' errors that change very slowly (seasonal) or remain totally unchanged during operation. Static errors are generally a residue of the initial adjustment of the lattice elements, e.g. random (gap to gap) RF amplitude errors from the field adjustment with bead pull ($\approx$ 1%), or random quadrupole gradient errors ($\approx$ 1%). While static errors usually change from element to element the dynamic errors tend to be grouped, originating from pulse to pulse variations of RF (< 1%, 1°) or quadrupole (< 0.5%) power supplies. For dynamic errors the search for worst case scenarios out of a large number of statistical runs is of little importance since normal machine operation will always yield average values. The same is true for certain static errors, like quadrupole gradient variations, which can be reduced with automated tuning systems. Some static errors, however, cannot be compensated for (e.g. residual field adjustment errors in multi-gap RF tanks) and for those the worst case results should be taken into account.
For the simulations uniform error distributions are used with a specified maximum error amplitude, meaning that the r.m.s. error values are obtained by multiplying the quoted maximum amplitudes by ≈ 0.58. To keep the computation time low, an RFQ output distribution with a low number of particles ($\approx$ 25000) is used. A preprocessor creates 300

random error sets, applies them to the original lattice and stores the new input files in scratch directories. With a simple shell script the jobs are then submitted to a Linux cluster (< 3h on 30 processors). The results are then evaluated with a combination of python scripts and fortran sub-routines.

Emittance Growth

In the transverse plane the grouping of quadrupoles typically involves around 5 magnets per power supply and it has been shown [3] that the emittance growth from grouped and ungrouped quadrupole errors is almost exactly the same. This was confirmed by simulations of the ESS front-end and therefore we only plot the results of one quadrupole error type (grouped) for different amplitudes. Fig. 8 shows the average additional emittance growth due to these errors.
The saturation in emittance growth for the largest values is possibly due to particle loss in the MEBT.
Figure 9 shows the additional average r.m.s. emittance growth for grouped and ungrouped RF errors as well as the maximum r.m.s. emittance growth for the latter error type.
Contrary to the common experience for linac structures, the plots show that the ungrouped random error distributions result in larger emittance increases than the grouped errors. Since the beam loss for both versions is almost exactly the same an explanation is not at all obvious at this stage and needs further study.

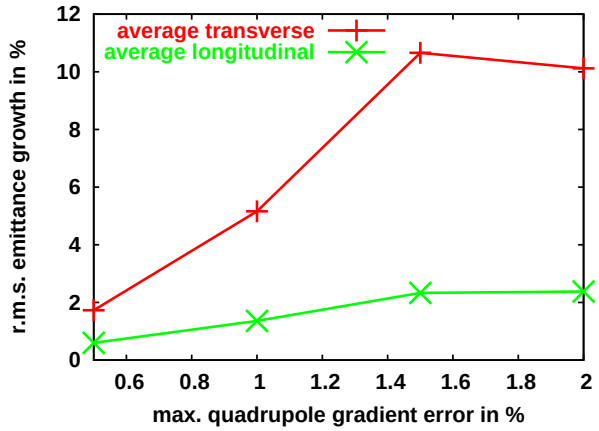

FIGURE 8. Additional average r.m.s. emittance increase for grouped quadrupole gradient errors in the ESS front-end.

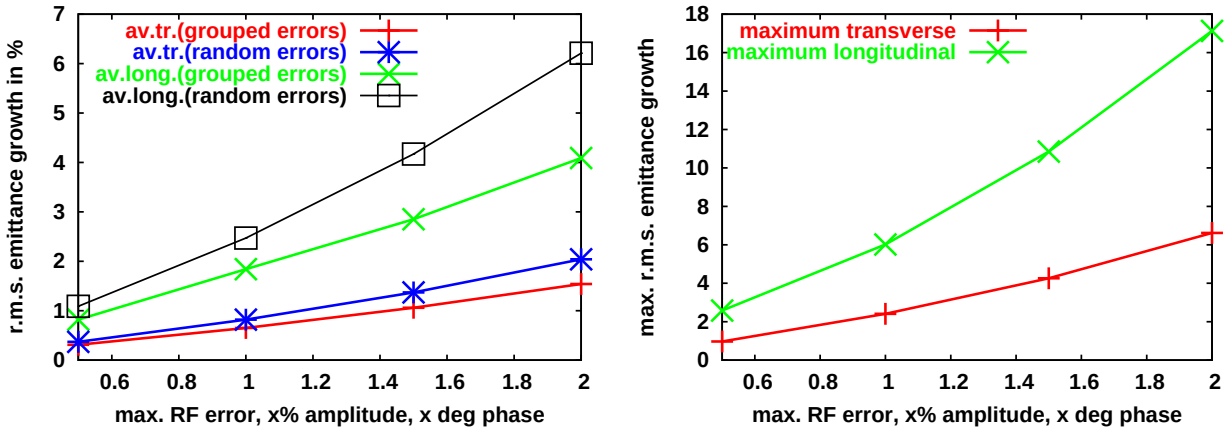

FIGURE 9. **Left:** average additional r.m.s. emittance increase for dynamic (grouped) and static (ungrouped) RF errors; **right:** maximum additional r.m.s. emittance growth for ungrouped RF errors.

Phase and Energy Jitter

In the case of the ESS front-end, phase and end energy jitter have to be controlled rigorously. The affected machine areas are first of all at the transition to 560 MHz at the beam funnel and secondly the injection into the ring systems. Since the phase and energy deviations caused by the static (ungrouped) errors can be compensated we plot only the effects of the dynamic grouped errors. Figure 10 shows the probability for energy and phase devitations at the linac end to be within distinct ellipsoidal areas of maximum phase and energy jitter for four different error levels.

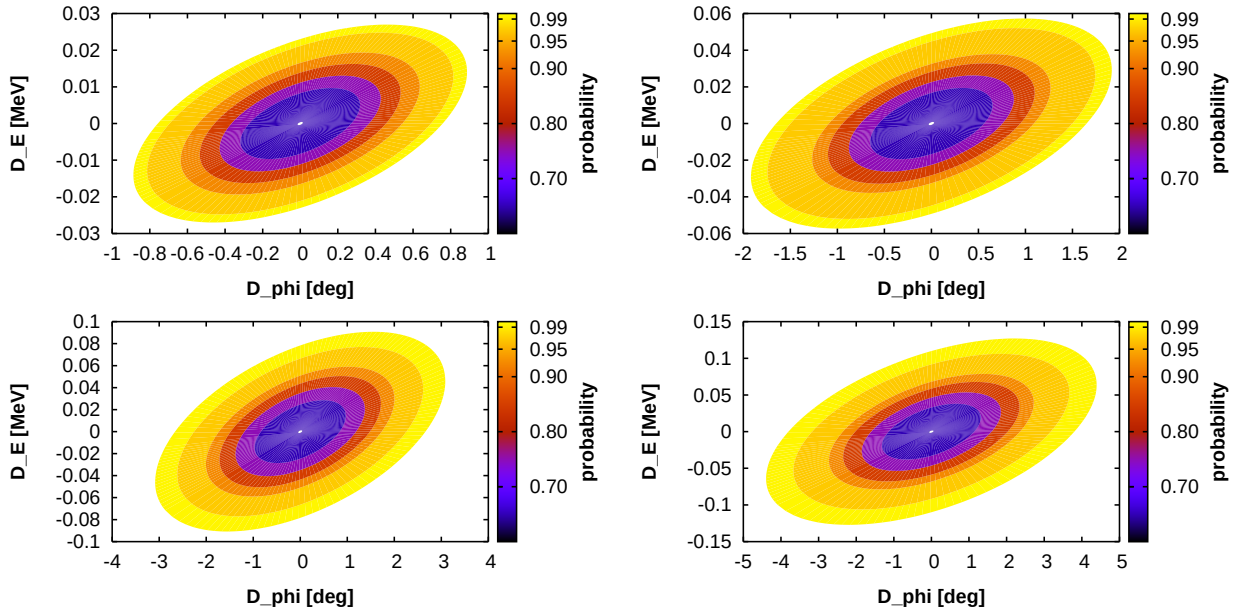

FIGURE 10. Probabilities for energy and phase deviation of the beam center at the end of the ESS front-end. Upper left to lower right: (0.5% max. field error, 0.5° max. phase error) → (1.0%, 1.0°) → (1.5%, 1.5°) → (2.0%, 2.0°).

Since the linac section under study is relatively short, the jitter probabilities are highly dependent on the end-plane of the simulation and are likely to change if the simulated linac is shortened or lengthened by a few focusing periods. This is illustrated by the worst case energy and phase deviations for maximum errors of 1% and 1° in Fig. 11. The deviations seem to form nodes where most of the minima occur. In our case the energy jitter at the end of the linac seems to represent the worst cases well while the phase jitter seems to reach much higher values in the middle of tank 2 than at the end of the linac. In the realistic machine it is unlikely that the nodes will be at exactly the same position, meaning that the worst case values should be considered for the design of the subsequent sections. For the ESS front-end we therefore recommend a tight RF control of 0.5% field error and 0.5° phase error.

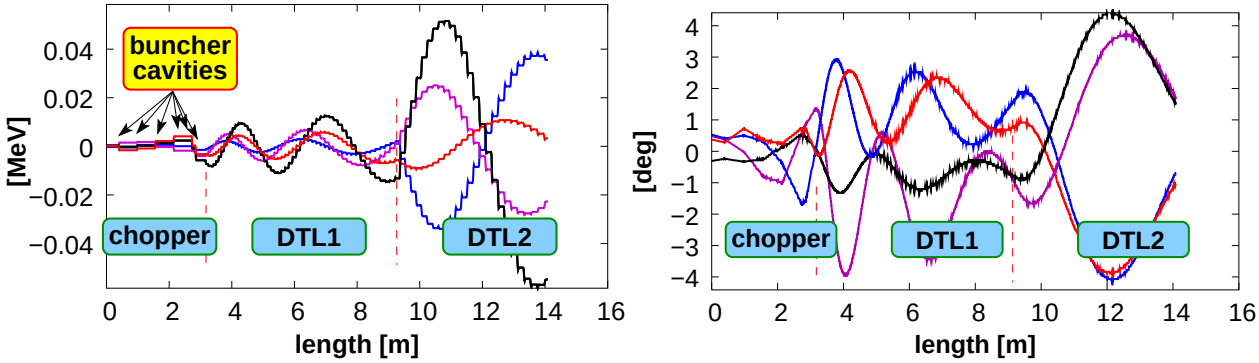

FIGURE 11. Total r.m.s. phase and energy width along MEBT and DTL.

Particle Loss Due To Statistical Errors

Initial mismatch and statistical errors yield deviations from the matched particle trajectories in all three planes. In case of initial mismatch, fairly regular oscillations of the beam trajectories around their equilibrium orbits are excited, while statistical errors result in much more irregular oscillations as shown for the longitudinal plane in Fig. 11. The outermost particles eventually hit the beam pipe and are lost, yielding activation of the material and requiring additional cooling capacity, e.g. for the drift tube quadrupoles. In the ESS-MEBT the chosen aperture represents a compromise between the contradicting demands of keeping the chopper plate voltage low and minimizing beam loss. The final value is based on Fig. 12 showing the total particle loss in the MEBT as a function of the chopper plate distance. For the chosen aperture of 16 mm the total beam loss amounts to 0.36 %, corresponding to an average heat load of $\approx$ 170 W distributed on the four plates (for the distribution of the losses compare with Fig. 13 and 14)[2]. Introducing RF errors barely changes the losses as can be seen in Fig. 13. With the introduction of quadrupole errors, the losses in the MEBT increase slightly with increasing

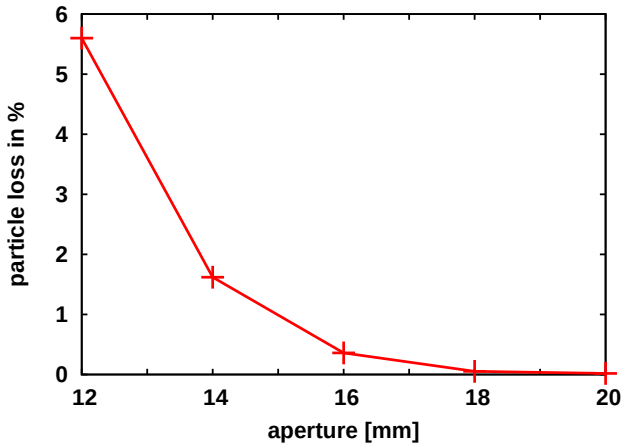

FIGURE 12. Total MEBT losses due to chopper plate distance.

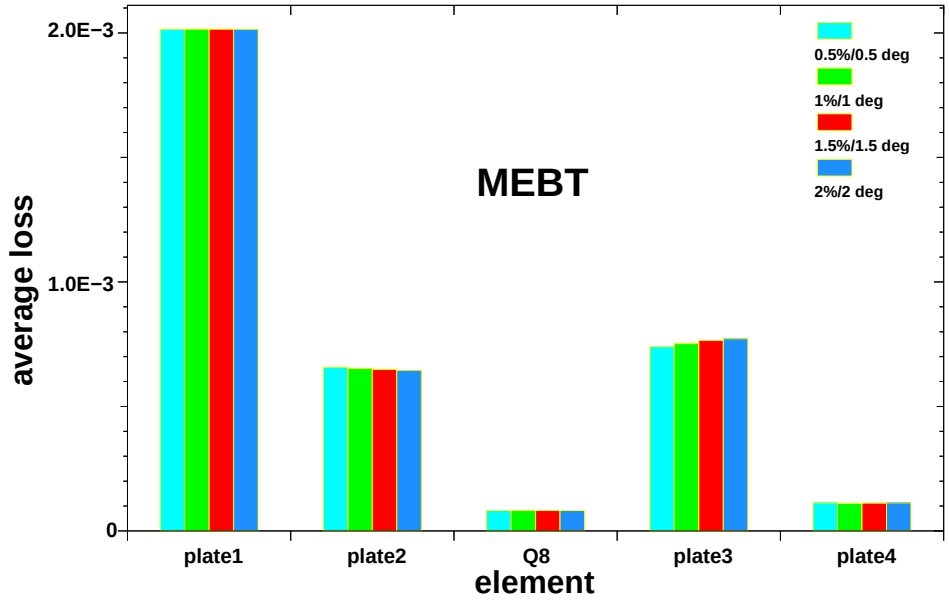

FIGURE 13. Particle loss due to statistical RF errors.

error amplitudes (see Fig. 14). The resulting losses in the subsequent DTL are approximately two orders of magnitude smaller and can only be seen in the zoomed in barchart in Fig. 15. Most of the losses in the quadrupoles are distinctly below the 0.001% level (< 50 mW) and fully comply with the requirements of low-loss machine operation.
Finally we compare losses in the DTL for 1% quadrupole gradient errors, when using the old (4.6) and new (6.5) ratios between r.m.s. beam size and beam pipe radius. The new FFDD lattice is used for both simulations, and the results are shown in Fig. 16. The losses due to this specific error type are reduced to almost zero, when the larger bore radius is

[2] The CERN design (Linac4), which is very similar to the ESS front-end, is based on 3% losses in the chopper line [10].

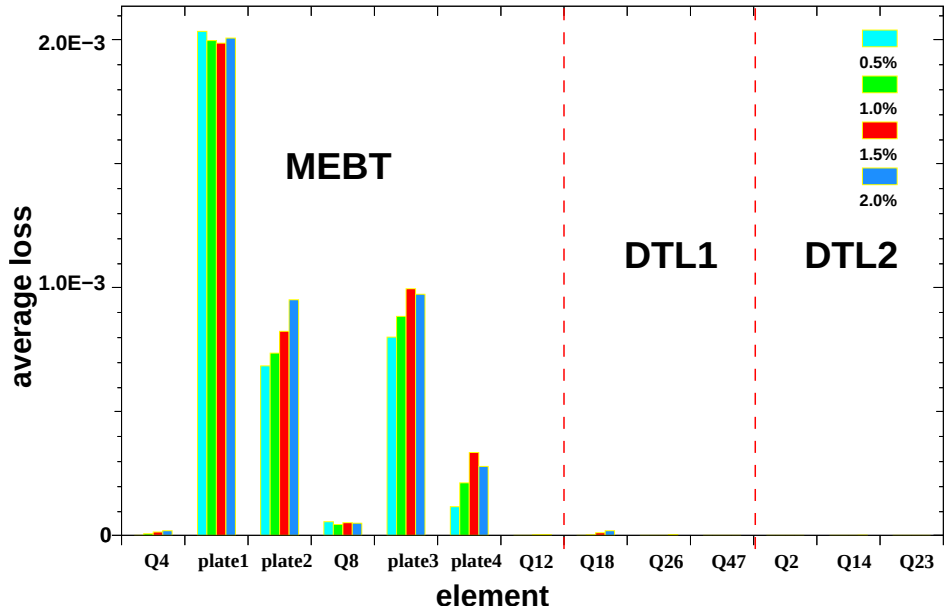

FIGURE 14. Particle loss due to statistical quadrupole gradient errors.

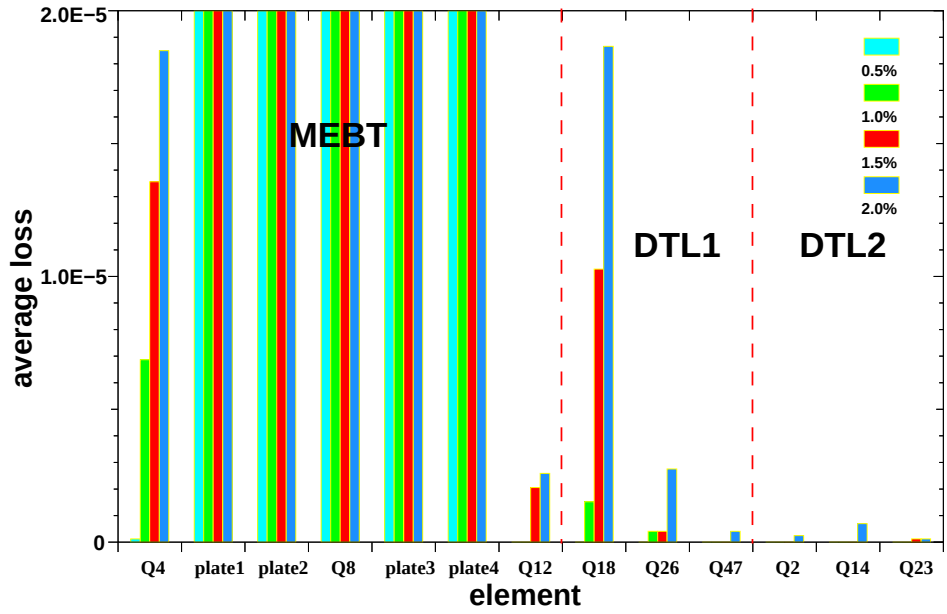

FIGURE 15. Particle loss due to statistical quadrupole gradient errors (zoomed in to see losses in the DTL quadrupoles).

used. Although the losses for the small bore still seem very small it should be noted that the real beam will not only suffer losses from quadrupole gradient errors, but also from alignment errors, transition mismatch between MEBT and DTL, rest gas-ionisation, residual fields between the chopper plates, ringing of the chopper RF system, etc. This means that Fig. 16 should not be considered in terms of absolute values but as a demonstration of the benefits of operating with a larger bore radius.

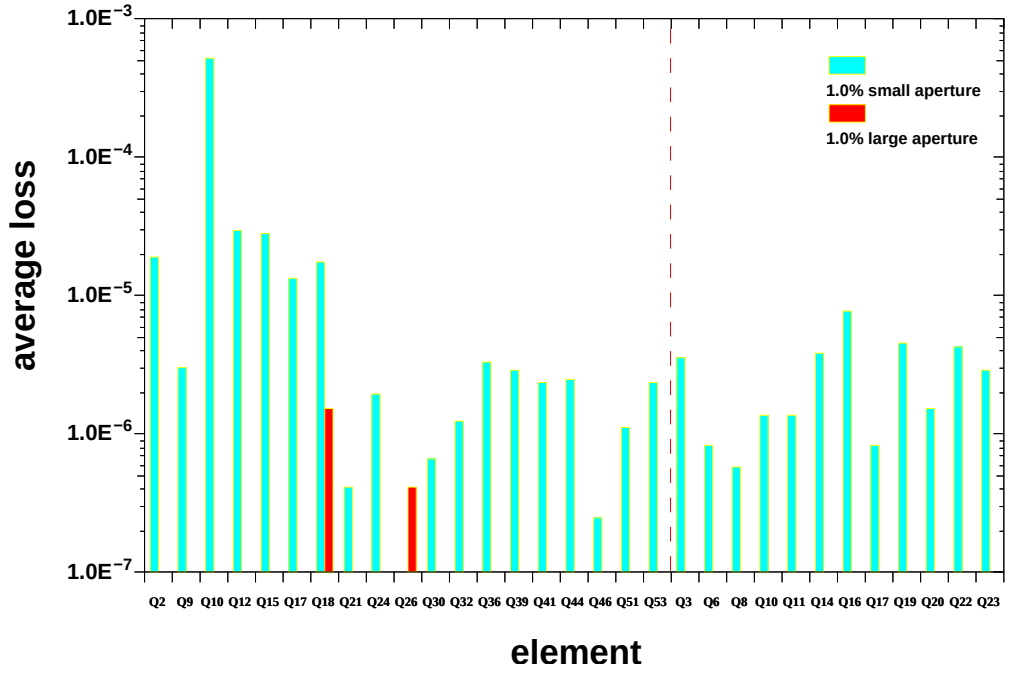

FIGURE 16. Particle loss due to 1% statistical quadrupole gradient errors for a DTL with large (6.5) and small (4.6) ratio between r.m.s beam radius and beam pipe radius.

SUMMARY AND OUTLOOK

The DTL design between the MEBT (2.5 MeV) and the beam funnel (20 MeV) has been revised in order to provide a larger safety margin between the r.m.s. beam radius and the radius of the beam pipe, and to relax the requirements for quadrupole alignment precision and quadrupole tip fields. Using roughly the same klystron power this is achieved by lengthening the DTL from 9.5 to 11 m, changing the focusing lattice from FD to FFDD, and changing the phase and energy ramps throughout the two tanks. Furthermore, a larger safety margin between the calculated shunt impedances and the quoted values was applied (20% instead of 10%). The MEBT was simulated with a realistic (simulated) RFQ output distribution and matched to the new DTL. In a future revision of the MEBT it might be useful to include adjustable scrapers in the layout that reduce the heat load on the first chopper plate and that are able to scrape in both transverse planes. The design philosophy for the RF and beam dynamics properties is outlined. A large number of statistical runs with IMPACT was performed to establish the beam properties for randomly distributed RF and quadrupole gradient errors. At this point the main concern is the limitation of energy and phase jitter at the end of the linac. For this purpose it seems necessary to control the RF to a level of 0.5% maximum gradient error and 0.5 deg maximum phase error. In the transverse plane, further results are needed for the beam sensitivity to alignment errors and transition mismatch before meaningful limits can be defined. Indications are, however, that a maximum quadrupole gradient error of 1%, which is comfortably within technological feasibility, will be sufficient for low-loss machine operation.

REFERENCES

1. Wangler, T., “Models and Simulation of Beam Halo Dynamics in High Power Proton Linacs,” in *ICAP98*, 1998.
2. Gerigk, F., Bongardt, K., and Hofmann, I., “High Current Linac Design with Examples of Resonaces and Halo,” in *LINAC02*, 2002.
3. Gerigk, F., “Halo Studies for the ESS and Linac4 Front-Ends,” in *HALO03*, AIP, 2003.
4. ESS Accelerator Team, *The ESS Project Volume III, Technical Report*, ISBN 3-89336-303-3, 2002.
5. Gerigk, F., and Vretenar, M., "Design Choices for the SPL Normal-Conducting Front End (3 - 120 MeV"), Tech. Rep. CERN-NUFACT-NOTE NF 110 (2002).
6. Billen, J. H., and Young, L. M., *Poisson Superfish V6*, LANL, LA-UR-96-1834, 2002.
7. Uriot, D., *DTL_GEN*, 2000.
8. Hofmann, I., *Physical Review E*, **57**, 4713–4724 (1998).
9. Qiang, J., Ryne, R. D., Habib, S., and Decyk, V., *Journal of Computational Physics*, **163**, 1–18 (2000).
10. Lombardi, A., private communications (2003).

APPENDIX A: MEBT PARAMETERS

TABLE 2. Simulated MEBT parameters, cavity voltage refers to E_0T, synchronous phase is $-90°$.

no.	element	length [mm]	value	aperture radius [mm]
1	**drift**	76.6		10
2	**quadrupole**	41.8	36.72 T/m	10
3	**drift**	56.2		10
4	**quadrupole**	41.8	-39.0 T/m	10
5	**drift**	96.2		10
6	**quadrupole**	41.8	55.0 T/m	10
7	**drift**	38.1		10
8	**RF-gap**		120 kV	10
9	**quadrupole**	41.8	-44.25 T/m	10
10	**drift (chopper)**	465.2		8
11	**quadrupole**	41.8	41.5 T/m	10
12	**drift**	18.1		10
13	**RF-gap**		66.2 kV	10
14	**drift**	18.1		10
15	**quadrupole**	41.8	-41.2 T/m	10
16	**drift (chopper)**	465.2		8
17	**quadrupole**	41.8	42.7 T/m	10
18	**drift**	18.1		10
19	**RF-gap**		84.3 kV	10
20	**drift**	18.1		10
21	**quadrupole**	41.8	-43.4 T/m	10
22	**drift (chopper)**	465.2		8
23	**quadrupole**	41.8	45.0 T/m	10
24	**drift**	18.1		10
25	**RF-gap**		108 kV	10
26	**drift**	18.1		10
27	**quadrupole**	41.8	-45.0 T/m	10
28	**drift (chopper)**	465.2		8
29	**quadrupole**	41.8	42.78 T/m	10
30	**drift**	18.1		10
31	**RF-gap**		78.5 kV	10
32	**drift**	37.6		10
33	**quadrupole**	41.8	-61.842 T/m	10
34	**drift**	37.6		10
35	**RF-gap**		134 kV	10
36	**drift**	37.6		10
37	**quadrupole**	41.8	27.911 T/m	10
38	**drift**	185.19		10

APPENDIX B: DTL PARAMETERS

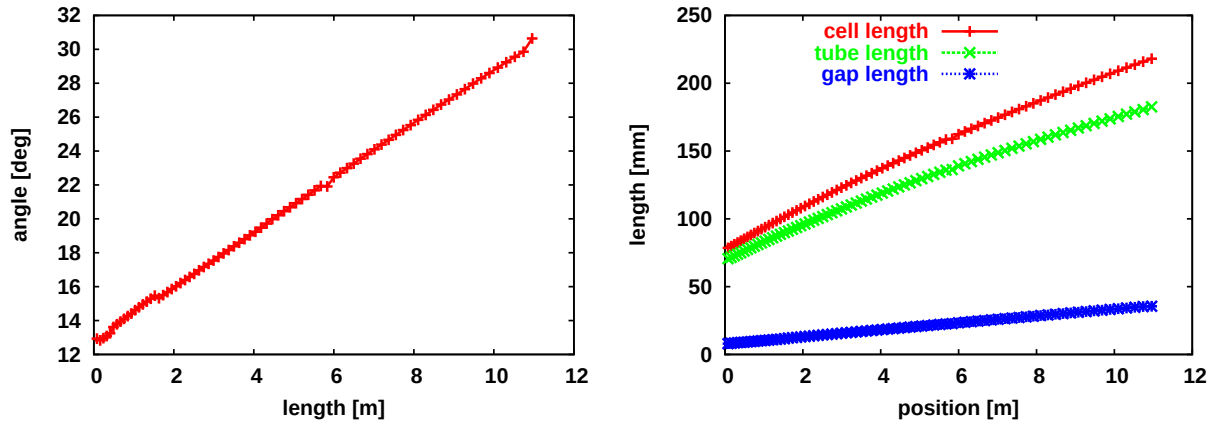

FIGURE 17. Geometric properties of drift tube cells along the two tanks. **Left:** drift tube face angles, **right:** cell, tube, and gap length.

TABLE 3. General DTL parameters.

	tank1	**tank2**	
W	2.497 → 11.4	→ 20.347	MeV
ϕ_s	-42 → -33.9	→ -30	deg
$\mathbf{E}_0$	1.8 → 2.23	→ 2.47	MeV/m
$\mathbf{P}_{copper}$	744	717	kW
$\mathbf{P}_{tot}$	1101	1074	kW
peak electric field	1.3	1.3	Kilpatrick
no. of gaps	52	25	
physical quadrupole length	45	60	mm
magnetic quadrupole length	40	52	mm
inner quadrupole radius	13	13	mm
tank length	6.2	4.7	m
tank diameter	570	570	mm
tube outer diameter	170	170	mm
stem diameter	30	30	mm
bore radius	11	11	mm
inner nose radius	3	3	mm
outer nose radius	8	8	mm
drift tube corner radius	5	5	mm
quadrupole gradient	46.5 → 38.5	31.0 → 27.0	T/m